Development of Cu$_{1.3}$Mn$_{1.7}$O$_4$ spinel coating on ferritic stainless steel for solid oxide fuel cell interconnects

N. Hosseini [a,*], M.H. Abbasi [a], F. Karimzadeh [a], G.M. Choi [b]

[a] Department of Materials Engineering, Isfahan University of Technology, Isfahan 84156-83111, Iran
[b] Fuel Cell Research Center and Department of Materials Science and Engineering, Pohang University of Science and Technology, Pohang 790-784, Republic of Korea

HIGHLIGHTS

- Cu$_{1.3}$Mn$_{1.7}$O$_4$ was prepared by glycine—nitrate process followed by mechanical milling.
- Cu$_{1.3}$Mn$_{1.7}$O$_4$ spinel layer was deposited on AISI 430 by screen-printing method.
- Cu$_{1.3}$Mn$_{1.7}$O$_4$ coating significantly retarded the sub-scale growth on AISI 430.
- The coating was crack-free and well bonded to the substrate after 500 h oxidation.
- The coating acted as a barrier to Cr diffusion and greatly reduced the ASR values.

ARTICLE INFO

ABSTRACT

To protect solid oxide fuel cells (SOFCs) from chromium poisoning and to improve area specific resistance (ASR), Cu$_{1.3}$Mn$_{1.7}$O$_4$ is thermally grown on AISI 430 ferritic stainless steel. The samples are characterized by X-ray diffraction (XRD), field emission scanning electron microscopy equipped with energy dispersive spectroscopy (FESEM-EDS) and 4-probe ASR tests. The results show that the coating not only decreases the ASR considerably, but also acts as a barrier to mitigate the sub-scale growth and to prevent chromium migration through the coating and the cathode. The EDS analysis reveals that a mixed spinel region is formed between the coating and oxide scale after 500 h oxidation at 750 °C causing a noticeable decrease in oxygen diffusivity through this layer and subsequent decline in sub-scale growth rate. The ASR of uncoated sample is measured to be 63.5 mΩ cm^2 after 500 h oxidation, while the Cu$_{1.3}$Mn$_{1.7}$O$_4$ spinel coated sample shows a value of 19.3 mΩ cm^2 representing ~70% reduction compared to the uncoated sample. It is proposed that the high electrical conductivity of Cu$_{1.3}$Mn$_{1.7}$O$_4$ (140 S cm^{-1}), reduction of oxide scale growth, and good bonding between the coating and substrate contribute to the substantial ASR reduction for the coated sample.

© 2014 Elsevier B.V. All rights reserved.

1. Introduction

Solid Oxide Fuel Cells (SOFCs) are promising candidates for new energy resources due to their low environmental impacts, high efficiency [1—4] and excellent fuel flexibility [4—6]. Direct conversion of chemical energy into electrical energy via electrochemical reactions between fuel and oxidant without involving combustion is the main characteristic of SOFCs [7,8]. As a key component of SOFCs stacks, interconnect provides electrical connection between single cells, physically separates the oxidant at the cathode and the fuel at the anode and distributes gases to the electrodes [9—13]. Consequently, interconnect materials must retain a series of requirements as follows: high temperature oxidation resistance and good stability in both reducing and oxidizing atmospheres, compatible thermal expansion coefficient (TEC) with the other parts of SOFCs stacks (cathodes, anodes and electrolytes), high electrical conductivity and marginal ionic conductivity [14—16], sufficient mechanical strength and creep resistance [15] and thermodynamic stability over the applied temperature range [16]. Recent progresses in manufacturing thinner electrolyte layers have reduced SOFCs operating temperatures from 950—1000 °C to 600—850 °C [5,16] making it possible to employ stainless steel interconnects instead of conventional doped lanthanum chromite

* Corresponding author. Tel.: +98 313 442 8591, +98 913 168 4752 (mobile); fax: +98 313 391 2752.
E-mail addresses: nazaneen_hosseini@ma.iut.ac.ir, nazaneen.4190@gmail.com (N. Hosseini).

($LaCrO_3$) ceramic components [17–23]. Among various stainless steels, chromia-forming ferritic stainless steels, e.g., type 430 alloy, Crofer22 APU, E-brite, ZMG 232 L etc, are promoted as the leading interconnect materials [1,24–28] because of their thermal expansion behavior close to ceramic parts, relatively high oxidation resistance, lower cost compared to ceramics [1,29,30], appropriate workability and machinability [5,30], structural integrity and high electrical and thermal conductivities [14]. However, these materials suffer from severe oxidation at the operating temperature of SOFC 600–850 °C during its expected long life (about 40,000 h) [31–33]. The continuous growth of oxide scale (consisting mainly of Cr_2O_3) with low electrical conductivity [10,12,15,34] increases the stacks electrical resistance [15–18,35–37] and the possibility of spallation because of the TEC mismatch between the oxide scale and the metallic substrate [36] and/or formation of porosity at the oxide scale/metallic substrate interface [11]. Another critical issue which limits the application of metallic interconnects is the evaporation of volatile Cr-rich species, i.e. CrO_3 or $CrO_2(OH)_2$, leading to rapid cathode performance degradation known as Cr-poisoning [37–44]. Upon combination with oxygen ions, the volatile Cr-rich species are reduced back to Cr_2O_3 and decrease the cathode active area [15,41]. It is worthy of consideration that the presence of $(Mn,Cr)_3O_4$ spinel top-scale with higher conductivity than Cr_2O_3 sub-scale, typically in type 430 alloy and Crofer22 APU [12,14,34,38,45,46], may reduce the contact resistance between the interconnect and the cathode or anode of SOFC [12,34]. This double-layer offers lower Cr-poisoning [12,14,34,40] because the chromium volatility in the spinel is smaller than Cr_2O_3 [14,19,41]. Nevertheless, previous study by Yang et al. [19] proved that considerable degradation of cell performance takes place for uncoated interconnects pointing to the significant chromium volatility from Cr-containing spinel layer particularly during the early stages of oxidation [47]. To overcome the drawbacks of metallic interconnects like Cr_2O_3 growth and Cr outward diffusion, and to improve the interface contact properties, they are usually coated by conductive ceramic oxides. The protective coating must have high electrical conductivity and low chromium cation and oxygen anion diffusivity at the operating temperature range of SOFCs [37]. As an alternate approach, conductive perovskites have been extensively used for such applications [48–54] due to their high conductivities and close matched TEC with alloys and electrode materials [1,7,55–57]. These coatings decrease the interfacial contact resistance [19,37,58]; however, high sintering temperature of the perovskites leads to low compaction of these coatings [7,11] and cell performance may still be degraded by outward chromium migration through the coating [19,37,59,60]. In addition to the perovskites, spinel oxides which contain no chromium can effectively retard oxidation and inhibit chromium volatility from ferritic stainless steels [4]. The most widely studied spinel to date is $(Mn,Co)_3O_4$ [33–35,61], while the $(Cu,Mn)_3O_4$ spinel system is a potential candidate for interconnect coating material owing to its excellent electrical conductivity [62] and compatible TEC with ferritic stainless steels [63]. Therefore, in the present study, $(Cu,Mn)_3O_4$ spinel layer, with a nominal composition of $Cu_{1.3}Mn_{1.7}O_4$, was thermally grown on AISI 430 ferritic stainless steel and its effectiveness in suppressing chromium migration and minimizing interfacial resistance was investigated for interconnect applications in intermediate temperature SOFCs.

2. Experimental

2.1. Coating deposition

Circular samples with dimensions of $\phi 18 \times 1$ mm were cut from commercial AISI 430 sheet steel using wire cutting. The chemical composition of the samples is presented in Table 1.

Table 1
Chemical composition of AISI 430 stainless steel.

Element	Cr	Mn	C	Si	S	P	Fe
Concentration (wt.%)	17.4	0.47	0.04	0.29	0.004	0.03	Balance

The sample surfaces were ground with SiC sand paper up to 600 grit. This procedure was executed to eliminate any surface defects and composition variation due to sheet processing, which could potentially influence the oxidation performance of the alloys. Prior to coating, any residue from the polishing process was removed by ultrasonic degreasing in an acetone bath for 15 min, rinsing with ethyl alcohol, and finally drying the samples in an oven at 67 °C.

$Cu_{1.3}Mn_{1.7}O_4$ spinel powder prepared by glycine–nitrate process (GNP) and subsequent mechanical milling was used as coating material. To do so, appropriate amounts of copper nitrate ($Cu(NO_3)_2 \cdot 3H_2O$, Sigma Aldrich, 98%), manganese nitrate ($Mn(NO_3)_2 \cdot 4H_2O$, Sigma Aldrich, 98%) and glycine (CH_2NH_2COOH, Sigma Aldrich, 98.5%) were dissolved into a small volume of deionized water to obtain transparent aqueous solutions. After 1 h of stirring, the solutions were heated on a hot plate using a large volume stainless steel beaker where the excess water was evaporated resulting in a viscous gel precursor. By increasing the temperature, an autoignition reaction spontaneously occurred in the precursor, upon which a large amount of gaseous phase was released. A voluminous black ash was formed, which was further crushed in a mortar. To remove any traces of glycine, nitrates and their undesirable decomposition products, the powders were subjected to calcination process at 500 °C for 2 h under argon atmosphere. To reduce the particle size and to break down the aggregates, the calcined powders were ball-milled for 1 h in a high-energy planetary mill (Fritsch, Mono mill Pulverisette 6 classic line model) using a zirconia vial containing zirconia balls and ethyl alcohol. The optimization of the $Cu_xMn_{3-x}O_4$ ($0.9 \leq x \leq 1.3$) spinel powders in terms of structural and electrical conductivity behavior is discussed in our previous study [62].

To prepare slurry of the coating, the synthesized powder was mixed with an appropriate binder. The slurry was applied onto the stainless steel samples by screen-printing method. After drying in an oven at 67 °C for 5 h, the coated and uncoated stainless steel samples were heat-treated in a quartz tube furnace under different conditions listed in Table 2.

To probe the chromium migration and subsequent Cr-poisoning of the cathode, the coated and uncoated AISI 430 samples were evaluated in a configuration (Fig. 1), which simulates interconnect/

Table 2
Different heat-treatment conditions for coated and uncoated AISI 430 samples.

| Sample	Heat-treatment conditions
A	Uncoated AISI 430 stainless steel oxidized at 750 °C for 100 h in air (Short-term oxidation)
B	Uncoated AISI 430 stainless steel oxidized at 750 °C for 500 h in air (Long-term oxidation)
C	$Cu_{1.3}Mn_{1.7}O_4$ spinel coated AISI 430 stainless steel oxidized at 750 °C for 100 h in air
D	$Cu_{1.3}Mn_{1.7}O_4$ spinel coated AISI 430 stainless steel reduced at 750 °C for 2 h in (Ar + 5% H_2)
E	$Cu_{1.3}Mn_{1.7}O_4$ spinel coated AISI 430 stainless steel reduced at 750 °C for 2 h in (Ar + 5% H_2) and oxidized at 750 °C for 10 h in air
F	$Cu_{1.3}Mn_{1.7}O_4$ spinel coated AISI 430 stainless steel reduced at 750 °C for 2 h in (Ar + 5% H_2) and oxidized at 750 °C for 100 h in air (short-term oxidation)
G	$Cu_{1.3}Mn_{1.7}O_4$ spinel coated AISI 430 stainless steel reduced at 750 °C for 2 h in (Ar + 5% H_2) and oxidized at 750 °C for 500 h in air (long-term oxidation)
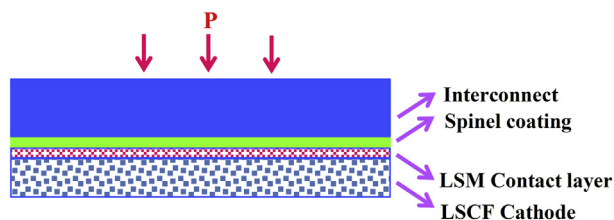
Fig. 1. Schematic illustration of interconnect/cathode interface in a SOFC stack.

cathode interface in SOFCs stacks. Porous LSCF ($La_{0.6}Sr_{0.4}Co_{0.2-}Fe_{0.8}O_3$) cathode ($\phi 18 \times 1$ mm) was prepared utilizing GNP followed by 2 h calcination at 850 °C, 2 h ball milling and sintering at 1040 °C in air. To prepare LSCF powder by GNP, appropriate amounts of lanthanum nitrate ($La(NO_3)_3 \cdot 6H_2O$, Samchun, 98%), cobalt nitrate ($Co(NO_3)_2 \cdot 6H_2O$, Sigma Aldrich, 98%), strontium nitrate ($Sr(NO_3)_2$, Sigma Aldrich, 99%), iron nitrate ($Fe(NO_3)_3 \cdot 9H_2O$, Katayama Chemicals, 98%) and glycine (CH_2NH_2COOH, Sigma Aldrich, 98.5%) were dissolved into deionized water. The aqueous solution was heated on a hot plate leading to the formation of a viscous gel. Further heating the viscous gel yielded to the formation of LSCF compound through an autoignition reaction. The calcination process was applied on the powder at 850 °C for 2 h in air. To reduce the particle size of the LSCF powder and making it suitable for sintering process, the powder was ball milled for 2 h in a high-energy planetary mill using a zirconia vial containing zirconia balls and ethyl alcohol. To obtain the LSCF porous cathode, the ball milled powder was then pelletized and sintered at 1040 °C for 2 h in air. A contact layer of LSM ($La_{0.8}Sr_{0.2}MnO_3$) slurry was applied on one side of the cathode by means of screen-printing. The LSCF cathode, screen-printed with the LSM wet coating, was applied on the reduced spinel coated sample. An isothermal oxidation test was subsequently performed at 750 °C up to 500 h. A simultaneous test was also considered for the uncoated interconnect/contact layer/cathode configuration for comparison.

2.2. Coating characterization

XRD analysis of the coated and uncoated samples as well as the cathodes was performed using XRD-Rigaku diffractometer (40 kV, 100 mA) with CuKα radiation ($\lambda = 1.54056$ Å). Surface morphologies and cross-sectional views of different samples were characterized by FESEM-EDS. Electrical performance of the coated sample was evaluated by standard 4-probe area specific resistance (ASR) test as a function of time at 750 °C for 500 h in air. Prior to ASR measurement, the coated sample was heat-treated in the reducing atmosphere at 750 °C for 2 h in reducing atmosphere (Ar + 5% H_2) and Pt meshes were fixed on both sides of the sample (Fig. 2) as current collectors. Moreover, Pt paste was applied between the meshes and the coated surface to improve the mesh to sample contact. The ASR includes the resistance of metallic substrate, the
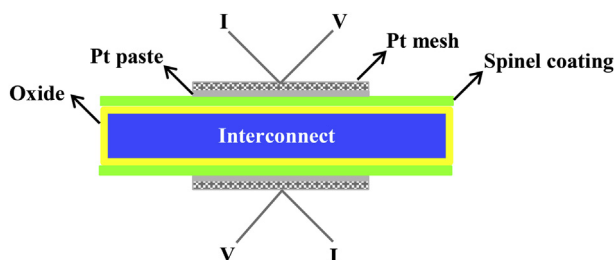
coating, and the oxide layer between the former two layers. Since the electrical resistance of the metallic substrate is negligible compared with the other two, the ASR measurement is a very effective way to reflect coating performance. For comparison, the electrical resistance of the uncoated sample was also measured as a function of time at 750 °C for 500 h in air.

3. Results and discussion

3.1. Microstructure

3.1.1. Uncoated AISI 430

Fig. 3 shows the XRD patterns of samples A and B. Samples A and B are the uncoated AISI 430 oxidized for 100 h and 500 h at 750 °C in air, respectively. The oxide phases including Cr_2O_3 and $(Mn,Cr,Fe)_3O_4$ spinel are present in both patterns. The relative ratio of $(Mn,Cr,Fe)_3O_4/Cr_2O_3$ peak intensities is increased with heat-treatment time indicating an increase in the spinel phase amount. Also, it is suggested that the fast growth of Cr_2O_3 is dominant in the first stage of oxidation, whereas the formation of spinel oxide governs the second oxidation stage to reduce the oxidation rate of the alloy [2]. According to the previous studies [17,18,64,65], the diffusion coefficient of metal ions in Cr_2O_3 layer grown on Fe–Cr alloys decreases in the order $D_{Mn} > D_{Fe} > D_{Ni} > D_{Cr}$ assuming that these ions diffuse via Cr^{3+}-lattice sites in Cr_2O_3. Consequently, the formation of $(Mn,Cr,Fe)_3O_4$ spinel on top of the Cr_2O_3 stems from high diffusion coefficient of Mn metal ions coming from the alloy to the Cr_2O_3 scale [17,66].

SEM images also reflect the changes in the scale grown on the surface of uncoated AISI 430. According to Fig. 4a (sample A), the scale appears discontinuous containing flaky Cr_2O_3 and dispersed prism-like $(Mn,Cr,Fe)_3O_4$ spinel particles. The EDS spectra from regions I (Fig. 4b) and II (Fig. 4c) confirm the presence of these two oxides, respectively (Fig. 4b and c). As for sample B, the surface is mainly covered by the loosely packed spinel crystals (Fig. 4d).

The cross-section morphology and corresponding EDS line scan of the sample B are presented in Fig. 5. Combined with the XRD results (Fig. 3), it is evident that there is a top-scale of $(Mn,Cr,Fe)_3O_4$ spinel over a Cr_2O_3 sub-scale. Mn is an important alloying element, which promotes spinel formation on top of the Cr_2O_3 scale [41] due to its high mobility and high oxidation potential [16]. The average thickness of the oxide scale on sample B was estimated to be ~4 μm.

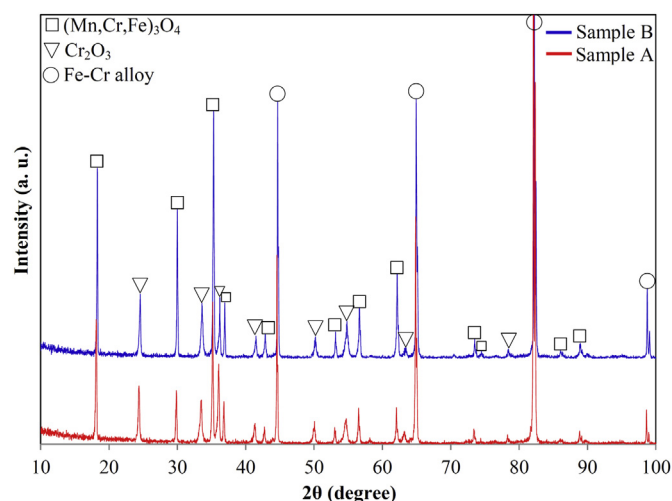**Fig. 2.** Schematic illustration of the setup used for ASR measurements.

Fig. 3. XRD patterns of the uncoated AISI 430 oxidized for 100 h (sample A) and 500 h (sample B) at 750 °C in air.
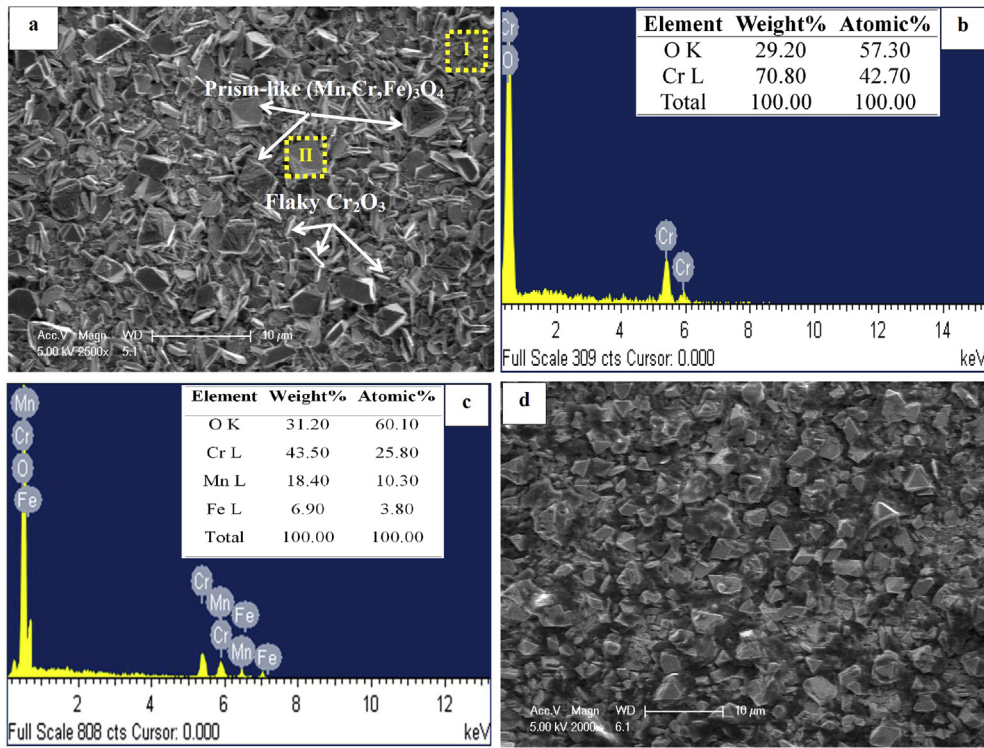
Fig. 4. SEM images for samples A (a) and B (d) and EDS spectra for regions I (b) and II (c) of sample A.

It is worth noting that the chromia-forming ferritic stainless steels with Cr content in the range of 15—20 wt.% exhibit considerable chromium vaporization in the working conditions of SOFCs. The vaporization of chromium species CrO_3 over Cr_2O_3 can be expressed as [67]:

$$Cr_2O_3(s) + \frac{3}{2}O_2(g) \leftrightarrow 2CrO_3(g) \tag{1}$$
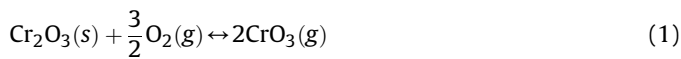
where the equilibrium constant, K, of this reaction is

$$K = \frac{P_{CrO_3}^2}{P_{O_2}^{3/2}} \tag{2}$$

where P_i is the partial pressure of the corresponding gas. The Van't Hoff equation is

$$\ln K = \frac{-\Delta H^0}{R}\left(\frac{1}{T}\right) + C \tag{3}$$

where ΔH^0 is the standard enthalpy change, R is the universal gas constant, T is temperature and C is a constant. Since the partial pressure of oxygen is fixed, combining Van't Hoff equation with Eq. (2) yields

$$\ln P_{CrO_3} = \frac{-\Delta H_r^0}{2R}\left(\frac{1}{T}\right) + C' \tag{4}$$

where ΔH_r^0 is the standard enthalpy change of reaction (1), and C' is a constant. When the surface of the scale is not $Cr_2O_3(s)$ and is covered by $(Mn,Cr,Fe)_3O_4$ spinel, the activity of $Cr_2O_3(s)$ at the surface is reduced; therefore, Eq. (4) is changed to
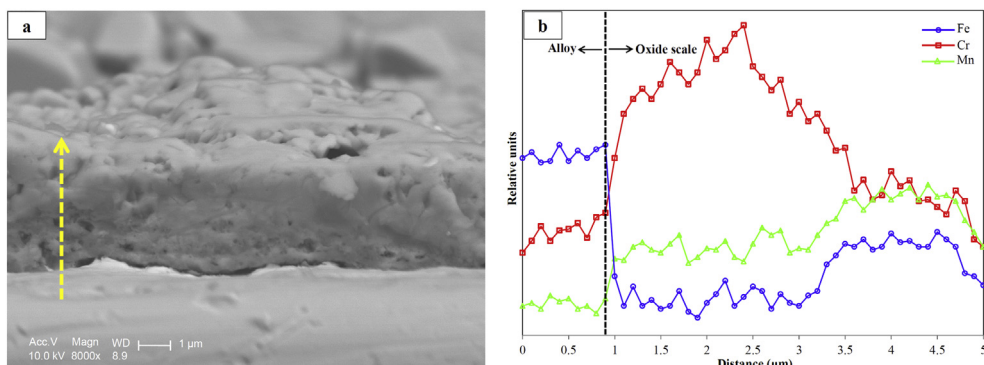

Fig. 5. SEM image for the cross-section (a) and EDS line scan (b) of sample B.

Table 3
TEC values for substrate and phases present in the oxide scale.

Material	TEC (10^{-6} C^{-1})	Temperature (°C)	Ref.
Cr_2O_3	9.6	(20–1000)	[5,11]
$MnCr_2O_4$	7.47	(100–900)	[13]
$MnFe_{0.1}Cr_{1.9}O_4$	9.57	(100–900)	[13]
$MnFeCrO_4$	9.93	(100–900)	[13]
Chromia-forming ferritic stainless steels	12	–	[2]
Chromia-forming ferritic stainless steels	11.9	–	[5]
Chromia-forming ferritic stainless steels	11–13	(20–1000)	[11]

$$\ln P_{CrO_3} = \frac{-\Delta H_r^0}{2R}\left(\frac{1}{T}\right) + C' + \ln a_{Cr_2O_3} \qquad (5)$$

where $a_{Cr_2O_3}$ is the activity of $Cr_2O_3(s)$ in the spinel phase. According to Eq. (5), the chromium vaporization is affected by the activity of $Cr_2O_3(s)$ at the surface of the scale. In the case of sample B (Fig. 5), $(Mn,Cr,Fe)_3O_4$ spinel formation as the top-scale reduces $a_{Cr_2O_3}$ and decreases the chromium vaporization [17,45]. However, by not protecting the substrate against the oxidation reactions, the double-layer scale significantly lowers the electrical conductivity of the SOFCs [17,68]. Also, investigations exhibit considerable TEC mismatch between the oxide scale and metallic substrate, which increases the thermal stresses and probable local spallation [11]. Table 3 compares the TEC values of Cr_2O_3, Mn–Cr spinels and chromia-forming ferritic stainless steels.

Fig. 6a illustrates the cross-section morphology of LSCF cathode in contact with the uncoated AISI 430 oxidized at 750 °C up to 500 h according to the configuration shown in Fig. 1. The presence of Cr (~4 at.%) in the EDS spectrum of region I (Fig. 6b) confirms the chromium migration toward the cathode side. In fact, the volatile Cr-rich species such as CrO_3 from oxidized scale is reduced at the electrochemical active sites of the cathode, thereby blocks the oxygen reaction sites [20,24,69] causing a considerable degradation of SOFC power [18].

3.1.2. $Cu_{1.3}Mn_{1.7}O_4$ coated AISI 430

The XRD pattern of sample C is shown in Fig. 7a. As shown, the protective coating consists of pure $Cu_{1.3}Mn_{1.7}O_4$ after 100 h oxidation signifying the phase stability of spinel phase at 750 °C.
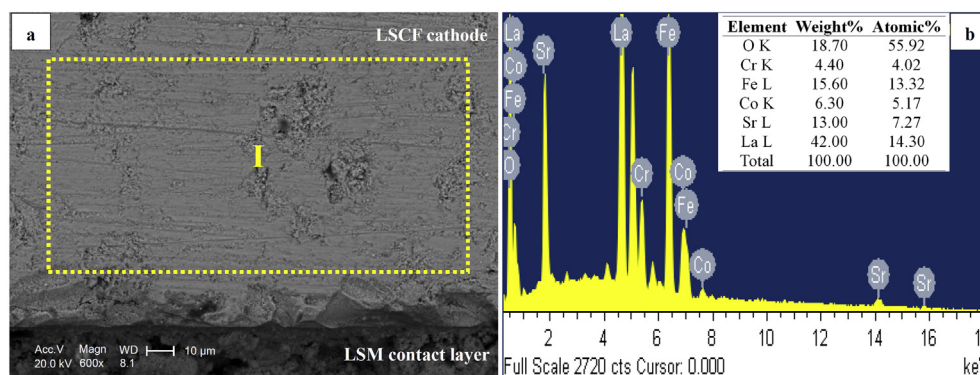
According to Fig. 7b, the microstructure of sample C is not fully dense and evidences of crack propagation are observed. Higher magnification of surface morphology is depicted in Fig. 7c. Randomly distributed prismatic spinel grains are clear. The cross-sectional view (Fig. 7d) also proves cracking and poor bonding between the coating and the substrate.

In order to improve the interfacial bonding between the spinel protective layer and the ferritic stainless steel and to achieve a dense coating, heat treatment in reducing atmosphere before exposure to the oxidation condition was applied on the coated samples. Fig. 8 shows the XRD pattern and SEM images for the surface of sample D (after 2 h heat treatment in Ar + 5% H$_2$ at 750 °C).

The XRD pattern in Fig. 8a reveals that during reduction treatment in Ar + 5% H$_2$ mixture, the spinel coating is reduced to MnO + Cu. Fig. 8b and c illustrate that the surface morphology of sample D is relatively uniform and porous. Moreover, the BSE micrograph confirms the coexistence of sub-micron MnO particles within the Cu matrix, respectively with bright and gray contrast (Fig. 8d).

The cross-sectional image and corresponding EDS line scan of sample D are presented in Fig. 9. As shown the coating is adhered well to the substrate and presents a more compacted structure compared to sample C. The metallic Cu existing within the MnO grains improves the sintering and densification during reduction step [5]. The EDS analysis (Fig. 9b) indicates a multilayer structure comprising the substrate with high Fe and Cr content, a ~3 μm thick Cu-rich metallic layer and a top-layer with high concentration of Cu and Mn. For Cu distribution, the alloy/coating interface is more potential sites since the metallic alloy is in contact with the metallic Cu phase [5]. Furthermore, the direct bonding between the metallic Cu and other elements, e.g., Fe, Mn and Cr, from the substrate can significantly enhance the coating adhesion to the AISI 430 substrate [3]. According to the EDS results, this multilayer structure contains very small amount of Cr.

Subsequent thermal oxidation of the Cu + MnO precursor layer in air at 750 °C for 10 h (sample E) leads to the reproduction of $Cu_{1.3}Mn_{1.7}O_4$ spinel coating and no significant evidences of pure metal and manganese oxide are observed, as confirmed by XRD pattern in Fig. 10a. Despite sample C, the surface morphology of sample E is homogenous, dense and crack-free and no spallation is observed on the surface (Fig. 10b) indicating the effective role of reduction pre-treatment to prevent cracking and spallation of the coating, in agreement with data reported in previous studies [14,70–72]. It should be noted that during oxidation in air, the reaction between the reduced coating and oxygen element can considerably decrease the porosity and a comparatively dense packing coating is achieved [3]. In comparison with Fig. 8c, the grain morphology is changed substantially exhibiting prismatic grains (~0.6 μm) with faceted planes. The coated sample was then subjected to short-term oxidation denoted as sample F. Again, all the XRD peaks are consistent with $Cu_{1.3}Mn_{1.7}O_4$ (not shown) similar to sample E signifying that no phase transformation is occurred in the coating during 100 h oxidation at 750 °C. The

Element	Weight%	Atomic%
O K	18.70	55.92
Cr K	4.40	4.02
Fe L	15.60	13.32
Co K	6.30	5.17
Sr L	13.00	7.27
La L	42.00	14.30
Total	100.00	100.00

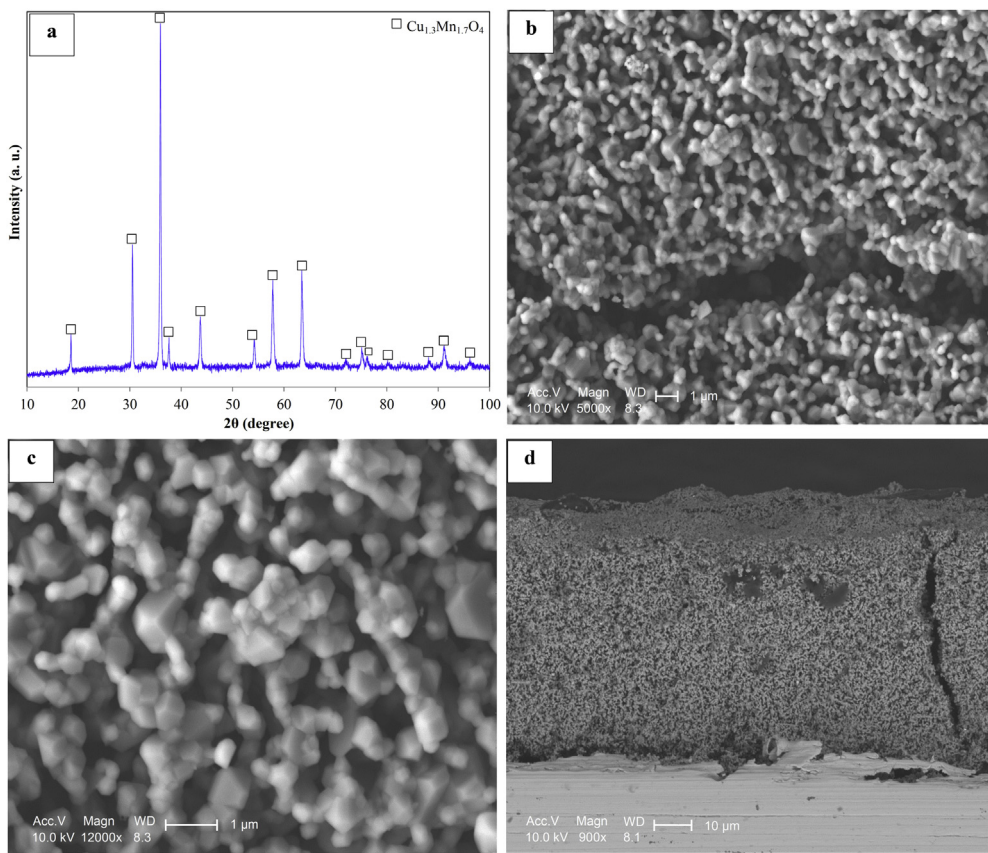**Fig. 6.** SEM image for LSCF cross-section (a) and EDS spectrum of region I (b).

Fig. 7. XRD pattern (a), SEM images of surface (b and c) and SEM image for the cross-section (d) of sample C.
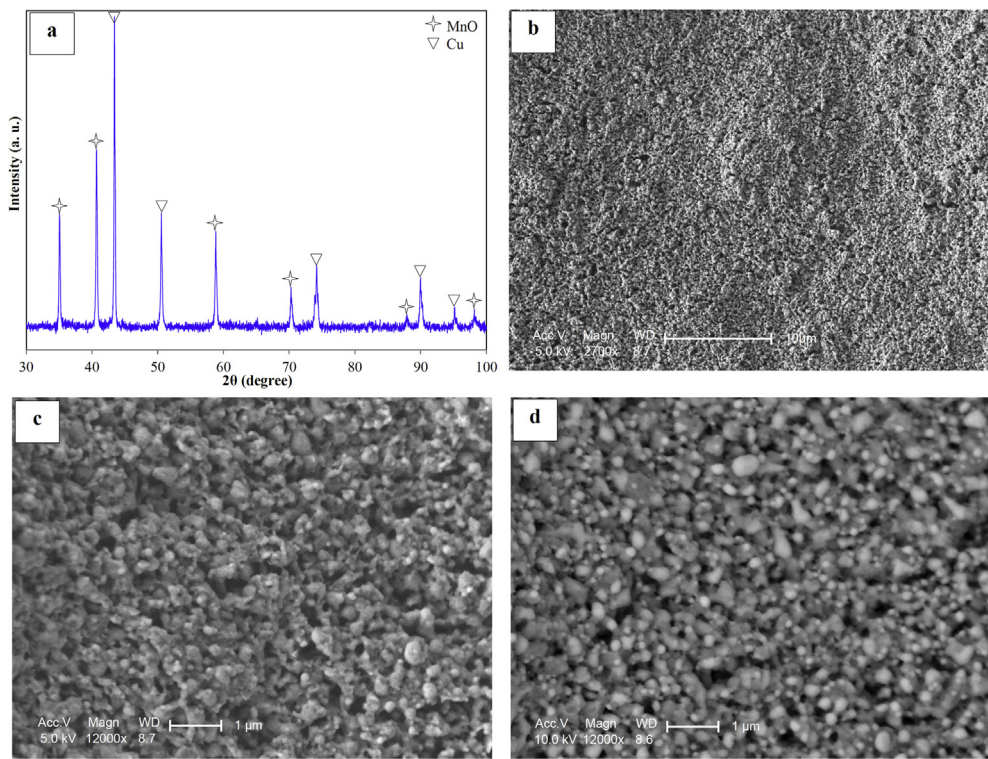

Fig. 8. XRD pattern (a), SEM images for the surface (b and c) and BSE image for the surface (d) of sample D.
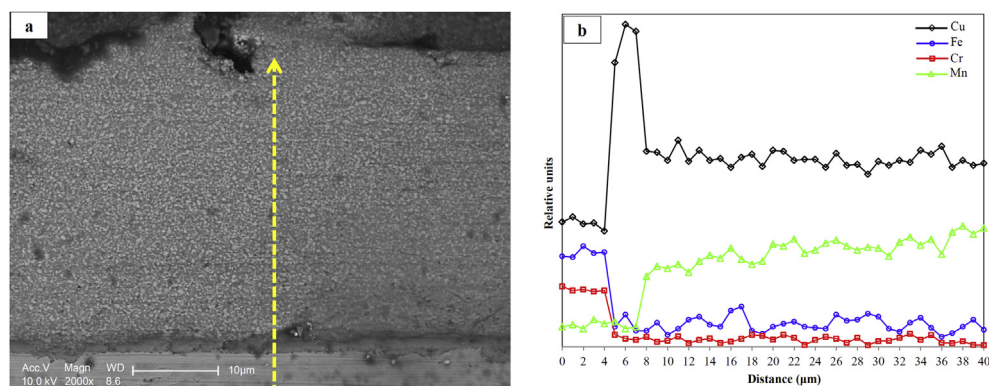
Fig. 9. SEM image for the cross-section (a) and EDS line scan (b) of sample D.

surface morphology and corresponding EDS spectrum of region I is depicted in Fig. 11. The surface morphology is the same as sample E, while the grain size is relatively increased with the average size of ~1 μm. Importantly, no chromium is detected on the surface of sample F (Fig. 11b) emphasizing the blocking nature of $Cu_{1.3}Mn_{1.7}O_4$ spinel coating.

According to Fig. 12a, the spinel coating has a closed-pores microstructure and well-bonded to the substrate via a continuous sub-scale. Moreover, the coating is free of cracks, spallation, or evidence of stress evolution. The EDS line scan (Fig. 12b) reveals that the Cr concentration increases markedly at the substrate/coating interface due to the formation of Cr_2O_3 sub-scale (~1 μm) followed by an abrupt drop in the spinel layer thickness. As illustrated in cross-sectional image (Fig. 12a), the interface of subscale/coating is smooth and continuous (Fig. 12a) and no detectable chromium penetration into the Cu/Mn-rich spinel layer has occurred (except ~2 μm beyond the subscale) during the short-term oxidation (Fig. 12b).

To assess the effectiveness of the spinel coating in suppressing the chromium diffusion, long-term oxidation (500 h at 750 °C) was executed on the coated sample (sample G). As shown in Fig. 13, the protective layer is made up of spinel phase and no indication of other phase is observed even after 500 h oxidation.

Surface morphology and the corresponding EDS spectrum of sample G are illustrated in Fig. 14a and b, respectively. As shown, the grains are substantially larger (average grain size: ~2.4 μm) but similar dense prismatic morphology can be observed in comparison with samples E and F. Furthermore, there is no chromium enrichment on the coating surface (Fig. 14b). Fig. 14c and d shows the cross-sectional image as well as EDS line scan of sample G. The

porosity appears to be lower than sample F indicating that longer exposure leads to further sintering of the spinel [58]. The spinel protective layer appears to have a good adhesion with the substrate and is free of spallation, cracking, and delamination. Compared to Fig. 12b, the spread in the peak width of Cr in the vicinity of the coating/substrate interface indicates the growth of the Cr_2O_3 sub-scale. A smooth and continuous interface is observed between the coating and the sub-scale that grow to a thickness of only ~2 μm after 500 h exposure in air. In comparison, on bare AISI 430 the scale can grow up to ~4 μm thickness under similar conditions (sample B, Fig. 5). Thus, the $Cu_{1.3}Mn_{1.7}O_4$ spinel coating on AISI 430 significantly reduces the scale growth rate, which requires the inward diffusion of oxygen ions through the coating [58]. According to the EDS line scan (Fig. 14d), the coating layer seems to be an effective barrier against outward diffusion of Cr and Fe cations. It should be noted that marginal diffusion of Cr ions to ~5 μm beyond the sub-scale is recorded in the EDS results (at a concentration significantly lower than for Cr_2O_3) suggesting the incorporation of chromium cations into the spinel structure and subsequent formation of mixed spinel region [7,18,41]. Badwal et al. [73] reported that in the case of oxide coatings containing at least one metal, M, selected from the transition series Mn, Fe, Co and Ni, an M−Cr spinel layer would develop between the metal substrate and the coating layer by the reaction of the coating with the chromium oxide formed on the substrate.

To evaluate the alloy-coating interaction, an understanding of the cations and anions transport processes occurring in this system is necessary. The growth rate of oxide scale can be determined by diffusion of cations and oxygen ions through the oxide scale and the oxide scale/alloy interface. According to Wargner's theory, the
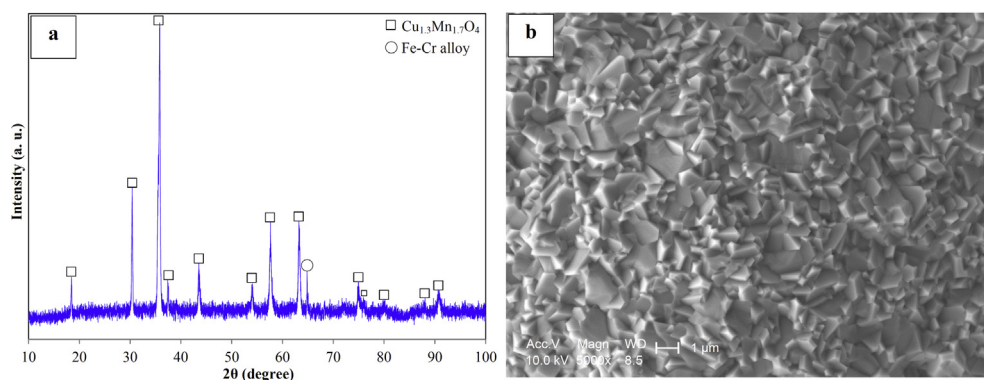

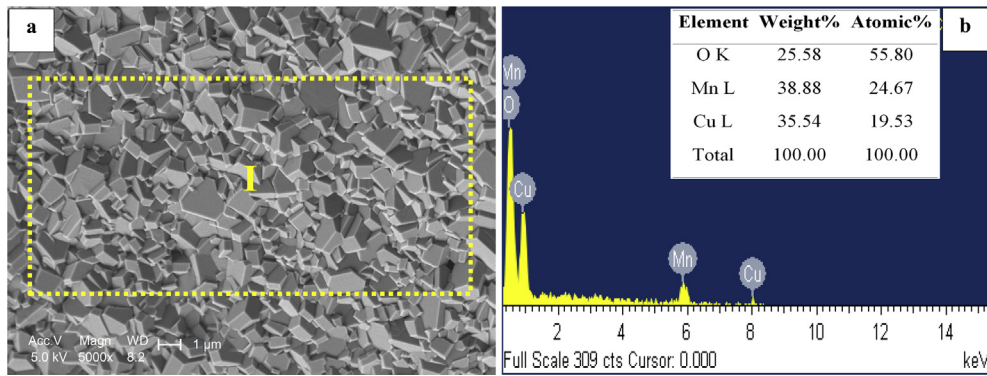**Fig. 10.** XRD pattern (a) and SEM image (b) of sample E.

Fig. 11. SEM image (a) and EDS spectrum (b) of sample F.

relationship between parabolic growth rate constant (k_p) and diffusion coefficients (cation and oxygen ions) is denoted by Eq. (6), assuming that the oxide scale mainly contains Cr_2O_3 [7,74]:

$$k_p = \frac{C_0}{2b} \int_{P'_{O_2}}^{P''_{O_2}} \left(\frac{3}{2} D_{cr} + D_0 \right) d\ln P_{O_2} \qquad (6)$$

where, D_{Cr} and D_O are the self-diffusion coefficients of Cr and O in the Cr_2O_3 scale, respectively. C_0 and b are constants. P'_{O_2} and P''_{O_2} are oxygen partial pressures at the atmosphere/oxide scale and oxide scale/alloy interfaces, respectively.

Considering Eq. (6), k_p for the oxide scale is dominated by the fastest diffusing ions. The diffusivity of Cr is reported to be faster than that of oxygen in Cr_2O_3-based oxides [7,75,76]. As a result, the oxidation of uncoated AISI 430 (samples A and B) is governed by chromium cation diffusion within the oxide scale. However, the oxidation kinetics of the $Cu_{1.3}Mn_{1.7}O_4$ coated samples is more complicated since the mixed spinel region affects the oxidation kinetics, particularly during long-term oxidation (sample G) [7]. During oxidation process, the chromium cations along with electrons transport toward the oxide scale/coating interface to react with oxygen ions and to form Cr_2O_3 oxide scale. As for bulk of the coating, the chromia scale is not formed on top of the coating (Fig. 13) and no chromium is penetrated to the surface of the coating (Fig. 14b) indicating faster diffusion of oxygen ions than chromium cations in the $Cu_{1.3}Mn_{1.7}O_4$ spinel coating [7]. By reaction of Cr_2O_3 scale and the spinel coating, the transport of oxygen ions is hindered in the mixed spinel region (Fig. 14d). Previous studies [7,75] have shown that the oxygen diffusivity is markedly

blocked in the Cr-rich oxide layer formed at the spinel coating/Cr_2O_3 oxide scale interface. Consequently, the chromium cations should further travel into the mixed spinel region to form the oxidation compounds. Considering all other parameters to be constant, increasing the distance that chromium cations should travel in this region exhibits the efficiency of the coating in suppressing the oxidation process [7]. Comparing samples F and G, it is obvious that higher thickness of mixed spinel region with low oxygen diffusivity causes a lower oxide scale growth rate.

The cross-section morphology of LSCF cathode in contact with the spinel coated AISI 430 oxidized at 750 °C up to 500 h is illustrated in Fig. 15. It should be noted that prior to oxidation, the coated sample is reduced separately for 2 h at 750 °C.

As evidenced by the EDS result, no chromium is detected in the LSCF cathode indicating the blocking nature of the $Cu_{1.3}Mn_{1.7}O_4$ coating during long term oxidation.

3.2. ASR measurements

Fig. 16 depicts the ASR values for AISI 430 with the $Cu_{1.3}Mn_{1.7}O_4$ spinel layer as a function of time at 750 °C. The coated sample was heat treated in Ar + 5% H_2 at 750 °C for 2 h before starting the test. For comparison, the ASR data for uncoated AISI 430 is also presented in Fig. 16 under similar conditions. In the case of uncoated sample, the contact ASR exhibits an initial rapid rise from 26 mΩ cm^2 to 51 mΩ cm^2 after only 100 h. As the time progresses, the ASR value is gradually increased to 63.5 mΩ cm^2. The noticeable increase in ASR for the uncoated AISI 430 is due to the continuous growth of oxide scale (Fig. 5) [1,17,38,77]. The conductivities of Cr_2O_3 sub-scale and $(Mn,Cr,Fe)_3O_4$ top-scale are markedly smaller compared to the metallic substrate [78]. In contrast to the uncoated
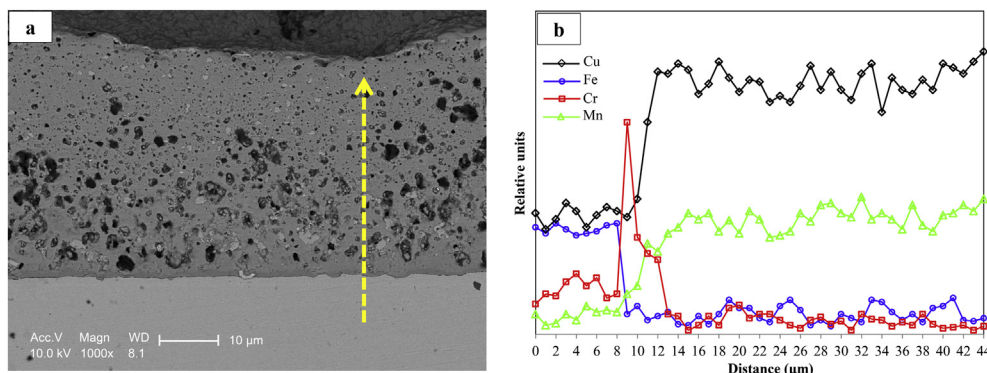

Fig. 12. SEM image for the cross-section (a) and EDS line scan (b) of sample F.
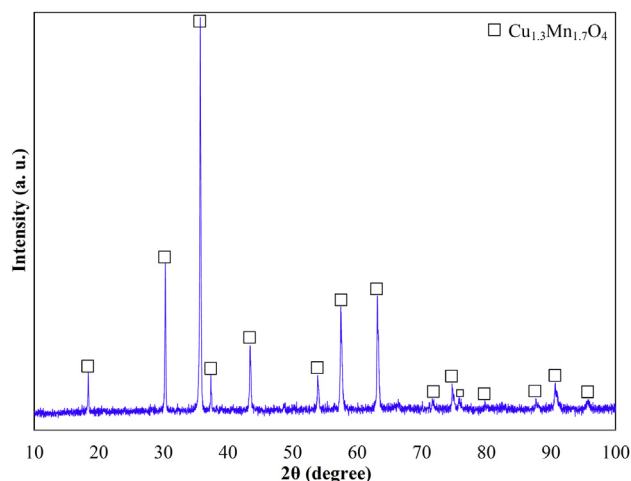
Fig. 13. XRD pattern of sample G.

sample, the $Cu_{1.3}Mn_{1.7}O_4$ coated AISI 430 shows extremely lower ASR values ranging from 15.1 mΩ cm^2 at the beginning to 19.3 mΩ cm^2 after 500 h oxidation at 750 °C.

The mechanisms by which the $Cu_{1.3}Mn_{1.7}O_4$ coated AISI 430 exhibits ~70% reduction in ASR after 500 h compared to uncoated AISI 430 can be explained from several aspects. First, the $Cu_{1.3}Mn_{1.7}O_4$ spinel has a high electrical conductivity value especially at 750 °C. The authors measured the electrical conductivity of $Cu_xMn_{3-x}O_4$ ($0.9 \leq x \leq 1.3$) dense pellets in their previous study [62], where the results showed that $Cu_{1.3}Mn_{1.7}O_4$ has the highest conductivity among the mentioned stoichiometries (140 S cm^{-1}). This value is significantly larger than those reported for the $(Mn,Cr)_3O_4$ [11,34,71,79,80] and Cr_2O_3 [5,16,80]. Second, the oxide

scale growth is considerably reduced causing a noticeable decline in the ASR values [16,19]. As discussed in the previous section, the existence of $Cu_{1.3}Mn_{1.7}O_4$ coating and particularly the mixed spinel region retards the oxygen diffusivity resulting in the lower oxide scale growth rate. Third, applying 2 h reduction treatment before the oxidation process, and formation of thinner Cr_2O_3 as well as good TEC matching between the $Cu_{1.3}Mn_{1.7}O_4$ (12×10^{-6} C^{-1} [63]) and the substrate (see Table 3) cause the coating to stay well-bonded to the substrate even after 500 h (Fig. 14c), which improves the ASR of the coated sample.

4. Conclusions

In this study, $Cu_{1.3}Mn_{1.7}O_4$ spinel layer was applied as the coating material on AISI 430 interconnects using reduction and subsequent oxidation heat treatment processes. The role of this coating in blocking the chromium diffusion and decreasing the ASR properties was investigated in the working conditions of intermediate temperature SOFCs. The results can be summarized as follows:

1 As for uncoated AISI 430 interconnect oxidized at 750 °C up to 500 h (sample B), the oxide scale with an average thickness of ~4 μm was formed including a top-scale of $(Mn,Cr,Fe)_3O_4$ spinel over a Cr_2O_3 sub-scale.
2 Reduction treatment for 2 h in Ar + 5% H$_2$ prior to 100 h and 500 h oxidation at 750 °C (samples F and G, respectively) yielded to the formation of crack-free coatings adhered well to the substrate via a thin Cr_2O_3 sub-scale.
3 No significant evidences of chromium migration to the surface and also along the thickness of samples F and G were found suggesting that the spinel coating layer acted as an effective barrier against outward diffusion of these cations.
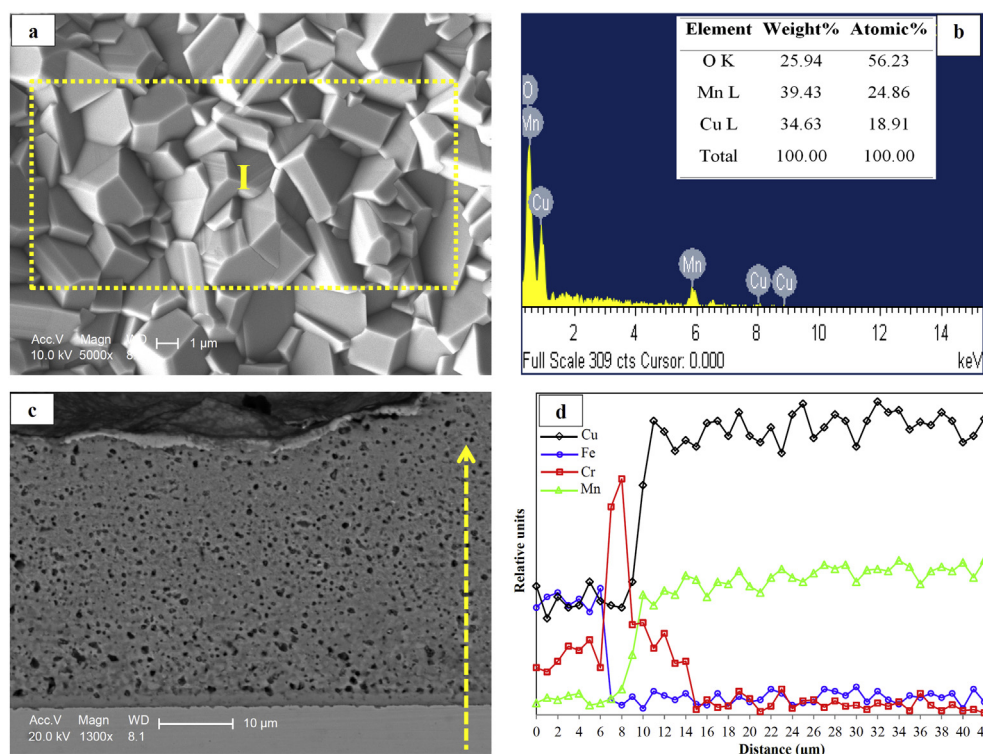

Fig. 14. SEM images for surface (a) and cross-section (c) and the corresponding EDS spectrum and line scan (b and d) of sample G.
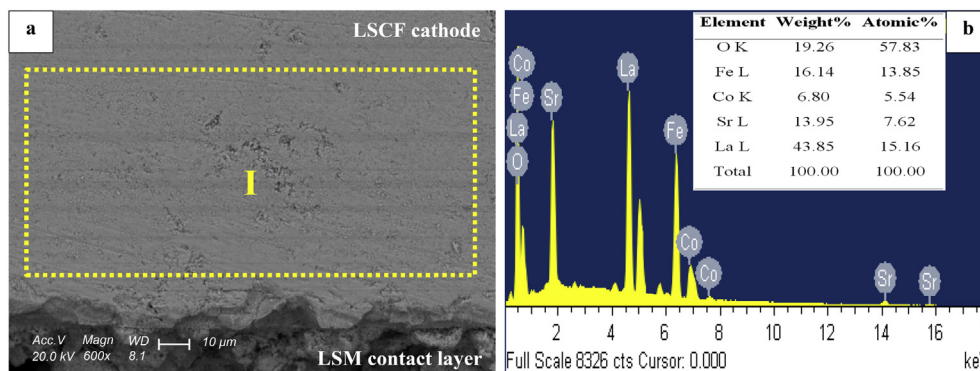
Fig. 15. SEM image for LSCF cross-section (a) and EDS spectrum of region I (b).
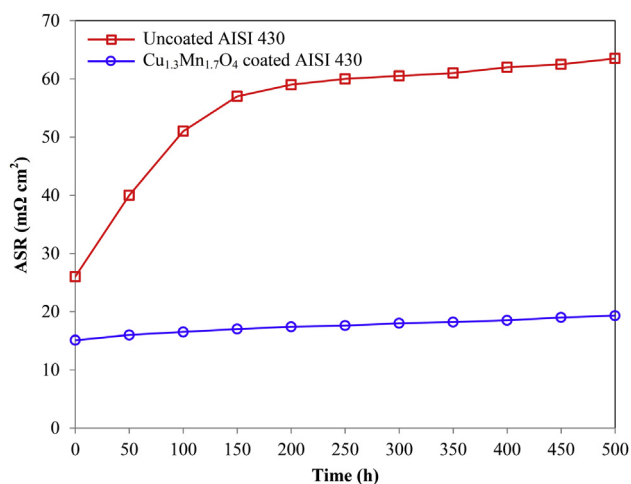

Fig. 16. ASR values for uncoated and coated samples as a function of time at 750 °C.

4 The presence of mixed spinel regions (samples F and G) significantly blocked the oxygen diffusion and reduced the oxide scale growth rate.

5 The ASR values for the uncoated AISI 430 increased from an initial value of 26 mΩ cm^2 to 63.5 mΩ cm^2 indicating a ~144% rise after 500 h. In contrast, the $Cu_{1.3}Mn_{1.7}O_4$ coated AISI 430 exhibited 19.3 mΩ cm^2 after 500 h, which is markedly lower than uncoated sample (~70%).

Acknowledgment

References

[1] Y. Xu, Z. Wen, S. Wang, T. Wen, Solid State Ionics 192 (2011) 561–564.
[2] D.R. Ou, M. Cheng, X.L. Wang, J. Power Sources 236 (2013) 200–206.
[3] X. Xin, S. Wang, J. Qian, C. Lin, Z. Zhan, T. Wen, Int. J. Hydrogen Energy 37 (2012) 471–476.
[4] P. Paknahad, M. Askari, M. Ghorbanzadeh, J. Power Sources 266 (2014) 79–87.
[5] N.J. Magdefrau, L. Chen, E.Y. Sun, J. Yamanis, M. Aindow, J. Power Sources 227 (2013) 318–326.
[6] W. Huang, S. Gopalan, U.B. Pal, S.N. Basu, J. Electrochem. Soc. 155 (2008) B1161–B1167.
[7] L. Chen, E.Y. Sun, J. Yamanis, N. Magdefrau, J. Electrochem. Soc. 157 (2010) B931–B942.
[8] C. Collins, J. Lucas, T.L. Buchanan, M. Kopczyk, A. Kayani, P.E. Gannon, M.C. Deibert, R.J. Smith, D.S. Choi, V.I. Gorokhovsky, Surf. Coat. Technol. 201 (2006) 4467–4470.
[9] J. Puranen, J. Lagerbom, L. Hyvärinen, T. Mäntylä, E. Levänen, M. Kylmälahti, P. Vuoristo, Surf. Coat. Technol. 205 (2010) 1029–1033.
[10] Y. Fang, C. Wu, X. Duan, S. Wang, Y. Chen, Int. J. Hydrogen Energy 36 (2011) 5611–5616.
[11] K. Wang, Y. Liu, J.W. Fergus, J. Am. Ceram. Soc. 94 (2011) 4490–4495.
[12] C.C. Mardare, H. Asteman, M. Spiegel, A. Savan, A. Ludwig, Appl. Surf. Sci. 255 (2008) 1850–1859.
[13] E. Stefan, J.T.S. Irvine, J. Mater. Sci. 46 (2011) 7191–7197.
[14] B. Hua, J. Pu, W. Gong, J. Zhang, F. Lu, L. Jian, J. Power Sources 185 (2008) 419–422.
[15] S.R. Akanda, M.E. Walter, N.J. Kidner, M.M. Seabaugh, J. Power Sources 210 (2012) 254–262.
[16] X. Chen, P.Y. Hou, C.P. Jacobsona, S.J. Visco, L.C.D. Jonghe, Solid State Ionics 176 (2005) 425–433.
[17] H. Ebrahimifar, M. Zandrahimi, Surf. Coat. Technol. 206 (2011) 75–81.
[18] J. Wu, C.D. Johnson, R.S. Gemmen, X. Liu, J. Power Sources 189 (2009) 1106–1113.
[19] Z. Yang, G. Xia, S.P. Simner, J.W. Stevenson, J. Electrochem. Soc. 152 (2005) A1896–A1901.
[20] W.Z. Zhu, S.C. Deevi, Mater. Sci. Eng. A 348 (2003) 227–243.
[21] J.W. Fergus, Solid State Ionics 171 (2004) 1–15.
[22] M. Dokiya, Solid State Ionics 383 (2002) 152–153.
[23] T. Brylewski, M. Nanko, T. Maruyama, Solid State Ionics 143 (2001) 131–150.
[24] J.W. Fergus, Mater. Sci. Eng. A 397 (2005) 271–283.
[25] K. Huang, P.Y. Hou, J.B. Goodenough, Solid State Ionics 128 (2000) 237–250.
[26] T. Horita, Y. Xiong, K. Yamaji, N. Sakai, H. Yokokawa, J. Electrochem. Soc. 150 (2003) A243–A248.
[27] T. Horita, Y. Xiong, K. Yamaji, N. Sakai, H. Yokokawa, J. Power Sources 118 (2003) 35–43.
[28] H. Kurokawa, K. Kawamura, T. Maruyama, Solid State Ionics 168 (2004) 13–21.
[29] I. Antepara, I. Villarreal, L.M. Rodríguez-Martínez, N. Lecanda, U. Castro, A. Laresgoiti, J. Power Sources 151 (2005) 103–107.
[30] T. Uehara, N. Yasuda, M. Okamoto, Y. Baba, J. Power Sources 196 (2011) 7251–7256.
[31] Z. Zeng, K. Natesan, Solid State Ionics 167 (2004) 9–16.
[32] N. Sakai, T. Horita, K. Yamaji, Solid State Ionics 177 (2006) 1933–1939.
[33] J. Wu, R.S. Gemmen, A. Manivannan, X. Liu, Int. J. Hydrogen Energy 36 (2011) 4525–4529.
[34] C.C. Mardare, M. Spiegel, A. Savan, A. Ludwig, J. Electrochem. Soc. 156 (2009) B1431–B1439.
[35] H. Abdoli, P. Alizadeh, Mater. Lett. 80 (2012) 53–55.
[36] W.N. Liu, X. Sun, E. Stephens, M.A. Khaleel, J. Power Sources 189 (2009) 1044–1050.
[37] W. Wei, W. Chen, D.G. Ivey, J. Power Sources 186 (2009) 428–434.
[38] Q.X. Fu, D. Sebold, F. Tietz, H.P. Buchkremer, Solid State Ionics 192 (2011) 376–382.
[39] S.P. Jiang, J.P. Zhang, L. Apateanu, K. Foger, J. Eletrochem. Soc. 147 (2000) 4013–4022.
[40] M. Stanislowski, E. Wessel, K. Hilpert, T. Markus, L. Singheiser, J. Electrochem. Soc. 154 (2007) A295–A306.
[41] J.W. Fergus, Scr. Mater. 65 (2011) 73–77.
[42] K. Fujita, T. Hashimoto, K. Ogasawara, H. Kameda, Y. Matsuzaki, T. Sakurai, J. Power Sources 131 (2004) 270–277.
[43] K. Fujita, K. Ogasawara, Y. Matsuzaki, T. Sakurai, J. Power Sources 131 (2004) 261–269.
[44] H. Tu, U. Stimming, J. Power Sources 127 (2004) 284–293.
[45] H. Kurokawa, C.P. Jacobson, L.C. DeJonghe, S.J. Visco, Solid State Ionics 178 (2007) 287–296.

[46] Z. Yang, M.S. Walker, P. Singh, J.W. Stevenson, T. Norby, J. Electrochem. Soc. 151 (2004) B669–B678.
[47] Z. Yang, G.G. Xia, G.D. Maupin, J.W. Stevenson, Surf. Coat. Technol. 201 (2006) 4476–4483.
[48] C.L. Chu, J.Y. Wang, S. Lee, Int. J. Hydrogen Energy 33 (2008) 2536–2546.
[49] C.L. Chu, J. Lee, T.H. Lee, Y.N. Cheng, Int. J. Hydrogen Energy 34 (2009) 422–434.
[50] C. Johnson, N. Orlovskaya, A. Coratolo, C. Cross, J. Wu, R. Gemmen, X. Liu, Int. J. Hydrogen Energy 34 (2009) 2408–2415.
[51] M.J. Tsai, C.L. Chu, S. Lee, J. Alloys Compd. 489 (2010) 576–581.
[52] S. Lee, C.L. Chu, M.J. Tsai, J. Lee, Appl. Surf. Sci. 256 (2010) 1817–1824.
[53] P. Yang, C.K. Liu, J.Y. Wu, W.J. Shong, R.Y. Lee, C.C. Sung, J. Power Sources 213 (2012) 63–68.
[54] T. Brylewski, J. Dabek, K. Przybylski, J. Morgiel, M. Rekas, J. Power Sources 208 (2012) 86–95.
[55] J.H. Zhu, Y. Zhang, A. Basu, Z.G. Lu, M. Paranthaman, D.F. Lee, E.A. Payzant, Surf. Coat. Technol. 177–178 (2004) 65–72.
[56] N. Orlovskaya, A. Corotalo, C. Johnson, R. Gemmen, J. Am. Ceram. Soc. 87 (2004) 1981–1987.
[57] D.P. Lim, D.S. Lim, J.S. Oh, I.W. Lyo, Surf. Coat. Technol. 200 (2005) 1248–1251.
[58] Z. Yang, G.G. Xia, J.W. Stevenson, Electrochem. Solid State Lett. 8 (2005) A168–A170.
[59] K. Hilpert, D. Das, M. Miller, D.H. Peck, R. Wei, J. Electrochem. Soc. 143 (1996) 3642–3647.
[60] Y. Larring, T. Norby, J. Electrochem. Soc. 147 (2000) 3251–3256.
[61] M.J. Lewis, J.H. Zhu, Electrochem. Solid State Lett. 14 (2011) B9–B12.
[62] N. Hosseini, F. Karimzadeh, M.H. Abbasi, G.M. Choi, Ceram. Int. 40 (2014) 12219–12226.
[63] N. Shaigan, W. Qu, D.G. Ivey, W. Chen, J. Power Sources 195 (2010) 1529–1542.
[64] M.G.E. Cox, B. McEnanay, V.D. Scott, Philos. Mag. 26 (1972) 839–851.
[65] R.E. Lobnig, H.P. Schmidt, K. Hennesen, H.J. Grabke, Oxid. Met. 37 (1992) 81–93.
[66] W. Qu, L. Jian, D.G. Ivey, J.M. Hill, J. Power Sources 157 (2006) 335–350.
[67] R. Trebbels, T. Markus, L. Singheiser, J. Electrochem. Soc. 157 (2010) B490–B495.
[68] Z.G. Yang, Int. Mater. Rev. 53 (2008) 39–54.
[69] J.W. Fergus, Int. J. Hydrogen Energy 32 (2007) 3664–3671.
[70] B. Hua, W. Zhang, J. Wu, J. Pu, B. Chi, L. Jian, J. Power Sources 195 (2010) 7375–7379.
[71] A.M. Dayaghi, M. Askari, P. Gannon, Surf. Coat. Technol. 206 (2012) 3495–3500.
[72] W. Zhang, J. Pu, B. Chi, L. Jian, J. Power Sources 196 (2011) 5591–5594.
[73] S. Badwal, K. Foger, X.G. Zheng, D. Jaffrey, US patent 5, 942, 349, August 24, 1999.
[74] A. Atkinson, Rev. Mod. Phys. 57 (1985) 437–470.
[75] T. Horita, H. Kishimoto, K. Yamaji, Y. Xiong, M.E. Brito, H. Yokokawa, Y. Baba, K. Ogasawara, H. Kameda, Y. Matsuzaki, S. Yamashita, N. Yasuda, T. Uehara, Solid State Ionics 179 (2008) 2216–2221.
[76] A.M. Huntz, S.C. Tsai, J. Mater. Sci. Lett. 13 (1994) 821–825.
[77] K. Huang, P.Y. Hou, J.B. Goodenough, Mater. Res. Bull. 36 (2001) 81–95.
[78] A. Holta, P. Kofstada, Solid State Ionics 69 (1994) 137–143.
[79] T. Sasamoto, N. Sumi, A. Shimaji, O. Yamamoto, Y. Abe, J. Soc. Mater. Sci. Jpn. 33 (1996) 32–37.
[80] C. Macauley, P. Gannon, M. Deibert, P. White, Int. J. Hydrogen Energy 36 (2011) 4540–4548.